Optik - International Journal for Light and Electron Optics 252 (2022) 168305

Contents lists available at ScienceDirect

Optik - International Journal for Light and Electron Optics

journal homepage: www.elsevier.com/locate/ijleo

Original research article

In silico evaluation of the effect of sensor directivity on photoacoustic tomography imaging

Pankaj Warbal, Ratan K. Saha *

Department of Applied Sciences, Indian Institute of Information Technology Allahabad, Prayagraj, 211015, India

ARTICLE INFO

MSC:
00-01
99-00

Keywords:
Directivity
Finite sensor
Photoacoustic tomography
Deblurring

ABSTRACT

The effect of sensor directivity on photoacoustic tomography (PAT) image reconstruction is examined. An analytical expression for the resultant PA signal, when emitted by an ensemble of spherical sources and detected by a planar sensor with finite aperture, is derived. This framework was employed to calculate the PA signal produced by a vasculature phantom containing many randomly distributed spherical sources mimicking the red blood cells (RBCs). A Monte Carlo algorithm was employed to generate the random locations of RBCs inside the vasculature. The calculated signals for many detector locations were utilized for image reconstruction via the Tikhonov regularization method. The corresponding system matrix was constructed in three ways by considering (i) sensors as point detectors (PDs), (ii) finite detectors but without directivity (FD WOD), and (iii) finite detectors with directivity (FD WD). The novelty of this work is to incorporate the effect of sensor directivity during the signal simulation as well as system matrix formation. The FD WD algorithm provided accurate image reconstruction while PD and FD WOD failed to recover the vascular structure. Pearson's correlation coefficient for the image formed using the FD WD technique was computed to be $\approx$ 4 times higher than that of the FD WOD method. The simulation results confirm that PAT imaging becomes independent of transducer directivity with the FD WD approach.

1. Introduction

The photoacoustic (PA) imaging couples the advantages of optics and acoustics [1,2]. The PA tomography (PAT) has emerged as a potential tool for sentinel-lymph node imaging [3,4], small animal brain imaging [5,6], molecular imaging [7,8], vasculature imaging [9,10], breast imaging [11,12] and tumor angiogenesis [13,14]. In PA imaging, tissue containing chromophores absorbs the optical energy when irradiated by short laser pulses and emits wide-band acoustic waves. This is because of the rapid thermo-elastic expansion of the illuminated region. These PA signals are captured using ultrasound detectors placed around the illuminated tissue. The recorded signals are then processed to generate the map of the initial pressure distribution. This is called image reconstruction. The reconstruction algorithms can be analytical as well as model-based. The analytical methods like backprojection (BP) [15–17] and time-reversal (TR) [18] algorithms are easy to implement and take less computational time (since they are noniterative in nature) to produce a reconstructed image. However, these methods are quantitatively less accurate. In general, images are corrupted with BP artifacts (e.g., streak artifact). Full view data set and filtering of the signals are required for faithful image creation reducing artifacts [19]. The model-based techniques (e.g., l_2 norm-based Tikhonov (TH) regularization, l_1 norm-based Tikhonov regularization and total variation minimization) are applied where limited view data set is available. They are computationally expensive

* Corresponding author.
E-mail address: ratank.saha@iiita.ac.in (R.K. Saha).
URL: https://profile.iiita.ac.in/ratank.saha/ (R.K. Saha).

https://doi.org/10.1016/j.ijleo.2021.168305
Received 24 July 2021; Received in revised form 22 October 2021; Accepted 6 November 2021
Available online 19 November 2021

(since generation and inversion of the system/model matrix are computationally expensive tasks) [20–23]. These algorithms can significantly suppress BP and various system-dependent (arising from the finite bandwidth of the transducers, finite apertures of the detectors, broad pulse width of the laser, acoustically lossy and dispersive medium) artifacts [20]. Therefore, they can facilitate quantitatively accurate reconstructed images.

Most PAT studies assume that the PA signals are captured by the point detectors having an omni-directional response. However, this assumption is not valid in practice. A real detector has a finite aperture size and its angular response is not uniform (rather direction-dependent) [24]. In general, in the far-field, the sensitivity of such a sensor is maximum along its axis and decreases gradually as the angle of the source point increases [24]. This gives rise to banding artifacts in the PAT images [25,26].

The effect of the sensor directivity on PAT imaging is investigated in the present work. For this purpose, we employed the discrete particle approach for signal simulation [27]. Essentially, tissue is hypothesized as an ensemble of discrete PA sources [e.g., blood can be considered as a collection of red blood cells (RBCs)], which emit PA signals upon illumination by the incident laser beam. Such a signal can be convolved with the spatial impulse response function (SIRF) of the detector. The linear superposition principle has been thereafter utilized to calculate the collective signal generated by many sources. Therefore, the effect of directivity of the sensor is included while simulating the forward data in this procedure. A simple analytical expression for the resultant PA signal can be derived for this theoretical framework.

Image reconstruction has been performed by implementing the Tikhonov regularization technique. The angular response of each sensor (of finite size) for each grid point has been incorporated while building the system matrix. This is referred to as FD WD in the remaining text. The reconstructed images created by this method have been compared with two other variants. In the first case, the system matrix has been formed by assuming detectors as point detectors (PDs). In the other case, only radial distances of the grid points from the centers of the sensors (of finite size) have been considered at the time of system matrix formation. This approach is mentioned as FD WOD in the following sections. Though this scheme considers finite size of the aperture, it does not include the directivity of the transducer. It is expected that the effect of directivity is canceled out during the matrix inversion process in the case of FD WD. Hence, the banding artifacts can be removed significantly in the reconstructed images. The effect of transducer directivity has also been examined for various scanning radii. To the best of our knowledge, the theoretical framework presented here, which incorporates the effect of sensor directivity during the signal simulation as well as system matrix formation, has never been performed in PAT studies. Therefore, the explicit inclusion of sensor directivity within the computations is the novelty of the work.

The organization of the paper is as follows. The forward and inverse frameworks are presented in the next section for signal simulation and image reconstruction, respectively. The simulation method is detailed in Section 3. Section 4 illustrates the results obtained in this study. The findings of this study are discussed in Section 4. The summary of the conclusions of this work is included in Section 5.

2. Forward and inverse frameworks

2.1. PA signal calculation for a finite detector

The PA field at a space point $\mathbf{r}$ generated by a light-absorbing sphere (with radius a and located at $\mathbf{r}_l$) under the conditions of thermal and stress confinements is given by [1],

$$\psi(\mathbf{r}) = BI_0 \left[\frac{[\sin(\hat{q}) - \hat{q}\cos(\hat{q})]e^{-ik_f a}}{\hat{q}^2[(1-\hat{\rho})\sin(\hat{q})/\hat{q} - \cos(\hat{q}) + i\hat{\rho}\hat{v}\sin(\hat{q})]} \right] \frac{e^{ik_f|\mathbf{r}-\mathbf{r}_l|}}{|\mathbf{r}-\mathbf{r}_l|}, \tag{1}$$

where $B = \frac{i\mu\beta v_s a^2}{C_P}$. Here, μ, β, and C_P represent the optical absorption coefficient, isobaric thermal expansion coefficient, and specific heat for the absorber; I_0 is the intensity of the incident radiation which is modulated with an angular frequency ω. Further, v_s and ρ_s are the sound-speed and density of the source, respectively. The same quantities for the ambient medium are denoted by v_f and ρ_f, respectively; $k_s = \omega/v_s$ and $k_f = \omega/v_f$ refer to the wave numbers inside and outside the PA source, respectively. The dimensionless quantities are defined as, $\hat{q} = k_s a$, $\hat{\rho} = \rho_s/\rho_f$, $\hat{v} = v_s/v_f$. If the illuminated region contains L number of spherical absorbers, the resultant PA field can be calculated using the linear superposition principle as,

$$\psi(\mathbf{r}) = \sum_{l=1}^{L} BI_0 \tilde{p}(\omega) \frac{e^{ik_f|\mathbf{r}-\mathbf{r}_l|}}{|\mathbf{r}-\mathbf{r}_l|}, \tag{2}$$

with

$$\tilde{p}(\omega) = \left[\frac{[\sin(\hat{q}) - \hat{q}\cos(\hat{q})]e^{-ik_f a}}{\hat{q}^2[(1-\hat{\rho})\sin(\hat{q})/\hat{q} - \cos(\hat{q}) + i\hat{\rho}\hat{v}\sin(\hat{q})]} \right].$$

The corresponding PA signal for a delta function heating pulse becomes,

$$\psi(\mathbf{r}, t) = \sum_{l=1}^{L} \frac{BF}{2\pi} \int_{-\infty}^{\infty} \tilde{p}(\omega) \frac{e^{ik_f|\mathbf{r}-\mathbf{r}_l|}}{|\mathbf{r}-\mathbf{r}_l|} e^{-i\omega t} d\omega, \tag{3}$$

where F is the fluence of the incident optical beam. The signal recorded by a finite detector can be expressed as,

$$\begin{aligned} P(t) &= \int\int_{S_{Area}} d^2\mathbf{r} \sum_{l=1}^{L} \frac{BF}{2\pi} \int_{-\infty}^{\infty} \tilde{p}(\omega) \frac{e^{ik_f|\mathbf{r}-\mathbf{r}_l|}}{|\mathbf{r}-\mathbf{r}_l|} e^{-i\omega t} d\omega \\ &= BF \sum_{l=1}^{L} \int_{-\infty}^{\infty} d\omega e^{-i\omega t} \tilde{p}(\omega) \int\int_{S_{Area}} \frac{e^{ik_f|\mathbf{r}-\mathbf{r}_l|}}{2\pi|\mathbf{r}-\mathbf{r}_l|} d^2\mathbf{r} \\ &= BF \sum_{l=1}^{L} \int_{-\infty}^{\infty} d\omega e^{-i\omega t} \tilde{p}(\omega) H_D(\omega), \end{aligned} \tag{4}$$

where $H_D(\omega) = \int\int_{S_{Area}} \frac{e^{ik_f|\mathbf{r}-\mathbf{r}_l|}}{2\pi|\mathbf{r}-\mathbf{r}_l|} d^2\mathbf{r}$ is the directivity function for the finite detector [28]; S_{Area} is the area of the aperture of the sensor. Eq. (4) further reduces to,

$$P(t) = \sum_{l=1}^{L} [p(t) * h(\mathbf{r}_l, t)], \tag{5}$$

where $*$ is the convolution operation with,

$$p(t) = \frac{BF}{2\pi} \int_{-\infty}^{\infty} \tilde{p}(\omega) e^{-i\omega t} d\omega, \tag{6}$$

and

$$h(\mathbf{r}_l, t) = \iint \frac{\delta(t - |\mathbf{r}-\mathbf{r}_l|/v_f)}{2\pi|\mathbf{r}-\mathbf{r}_l|} d^2\mathbf{r}, \tag{7}$$

is the SIRF of the transducer. In this work, Eq. (5) has been evaluated to calculate the resultant PA signal generated by a uniformly illuminated collection of light-absorbing spheres.

2.2. Image reconstruction

The PAT image reconstruction problem can be mathematically presented as a system of linear equations as [21],

$$M\mathscr{U} = P, \qquad M \in \mathbb{R}^{m\times n}, \quad P \in \mathbb{R}^m \quad \text{and} \quad \mathscr{U} \in \mathbb{R}^n \tag{8}$$

where M is the system/model matrix [27] that retains the properties of the medium, laser source, and acoustic sensors; P is a long column vector containing measured pressure data. Here, $\mathscr{U}$ is also a long column vector that essentially contains the spatial distribution of initial pressure rise within the imaging region due to the absorption of light. It is easy to obtain a unique solution of Eq. (8) when M is invertible (i.e., $m = n$, $|A| \neq 0$). If this condition is not met (e.g., $m > n$), a solution can be obtained by deploying the method of least squares such as,

$$\mathscr{U}_{sol} = \arg \min(\|M\mathscr{U} - P\|_2^2), \tag{9}$$

where $\|-\|_2$ is the l_2 norm. However, for discrete ill-posed problems the conventional methods for numerically solving Eq. (9) may not provide meaningful approximate solutions [29].

The standard approach for solving Eq. (8) is to employ the Tikhonov regularization method when $m \neq n$ [30]. The solution for this technique becomes [22],

$$\mathscr{U}_{sol} = \arg \min(\|M\mathscr{U} - P\|_2^2 + \lambda^2\|Q\mathscr{U}\|_2^2). \tag{10}$$

Here, λ is the regularization parameter; $Q \in \mathbb{R}^{n\times n}$ is the regularization matrix. It may be an identity matrix such as $Q = I$ or a high-pass/difference operator. The first term of the right hand side of Eq. (10) is termed as the fidelity term and the second term is called the penalty term. It is apparent from Eq. (10) that λ determines the enforcement of the penalty term while obtaining the solution. The over smoothening of the image happens at higher regularization whereas, at lower λ values, noise in the image gets amplified. The choice of the λ can be made manually (via visual inspection). It can also be made using some automatic techniques such as L-curve, generalized cross-validation (GCV) methods, etc.

The result of the minimization in Eq. (10) for $Q = I$ is written as,

$$\mathscr{U}_{sol} = (M^T M + \lambda^2 I)^{-1} M^T P, \tag{11}$$

where I being the identity matrix and T is the transpose operator. Eq. (11) can be further manipulated in the following manner to obtain a simple expression. For instance, the singular value decomposition (SVD) of M is given as,

$$M = U\Sigma V^T = \sum_{i=1}^{n} u_i \sigma_i v_i^T, \tag{12}$$

when $m \geq n$; $U = (u_1, u_2, \ldots, u_n)$ and $V = (v_1, v_2, \ldots, v_n)$ are the left and right orthogonal matrices, respectively; that is $U^T U = V^T V = I_n$; $\Sigma = \text{diag}(\sigma_1, \sigma_2, \ldots, \sigma_n)$ contains the non-negative diagonal elements or singular values in the descending order such that,

$$\sigma_1 \geq \sigma_2 \geq .... \geq \sigma_n. \tag{13}$$

Substituting Eq. (12) into Eq. (11) we get,

$$\begin{aligned}\mathscr{U}_{sol} &= (V\Sigma^T\Sigma V^T + \lambda^2 I)^{-1} V\Sigma^T U^T P \\ &= (V\Sigma^T\Sigma V^T + \lambda^2 VV^T)^{-1} V\Sigma^T U^T P \\ &= V(\Sigma^T\Sigma + \lambda^2)^{-1}\Sigma^T U^T P \\ &= \sum_{i=1}^{n} \frac{\sigma_i (u_i^T P)}{\sigma_i^2 + \lambda^2} v_i. \end{aligned} \tag{14}$$

The term $\frac{\sigma_i}{\sigma_i^2+\lambda^2}$ is called the filter factor. The filter factors remove the contributions from the small singular values, however, those of large singular values are retained unaffected.

The regularization matrix can be constructed involving a spatial derivative filter [22]. For example, normalized spatial Laplacian filter can be used having the following kernel [22],

$$K_L = \frac{1}{9}\begin{bmatrix} -1 & -1 & -1 \\ -1 & 8 & -1 \\ -1 & -1 & -1 \end{bmatrix}. \tag{15}$$

In this work, the regularization matrix has been built using the kernel K_L.

3. Simulation method

3.1. Numerical phantom

A binary image of a blood vasculature of size 20 × 20 mm^2 was scanned at 600 dots per inch providing 473 × 473 pixels. At first, the pixels containing the vasculature were identified and tagged as 1; other pixels were assigned as 0. The vasculature covered an area of ≈ 44 mm^2. A total number of 663609 RBCs approximated as spheres (with radius, a = 2.92 μm) were randomly placed within the pixels with tag 1. The random sequential adsorption (RSA) technique, a popular Monte Carlo algorithm for disk/sphere packing, was used for this purpose [31,32]. The cells did not overlap with other cells inside the same pixel as well as those of the neighboring pixels. The total area occupied by the RBCs was about 17.8 mm^2. Therefore, the hematocrit level became nearly 0.4. The procedure is also detailed in [27,31]. Tissue simulation consumed about 115 s in a virtual machine [CentOS, Intel Core Processor (Broadwell, IBRS), 2.19 GHz, 256 GB RAM, and 80 cores]. The vasculature phantom is presented in Fig. 1(a). It could be considered as a 2D sheet of a 3D tissue.

Note that the coordinates of RBCs were initially generated with respect to the X_0-Y_0 frame. For example, the coordinates for the lth cell were denoted by (x_{0l}^c, y_{0l}^c) as shown in Fig. 1(b). The coordinates for the same cell relative to the X_s-Y_s frame could be easily obtained and subsequently, those values (x_{sl}^c, y_{sl}^c) with respect to the detector D_s were computed. The formula for coordinate transformation is given below,

$$\begin{bmatrix} x_{sl}^c \\ y_{sl}^c \end{bmatrix} = \begin{bmatrix} r_d \\ 0 \end{bmatrix} + \begin{bmatrix} \cos(\pi+\theta_s) & \sin(\pi+\theta_s) \\ -\sin(\pi+\theta_s) & \cos(\pi+\theta_s) \end{bmatrix} \begin{bmatrix} x_{0l}^c \\ y_{0l}^c \end{bmatrix}, \tag{16}$$

where r_d is the scanning radius and the detector D_s makes an angle θ_s with the X-axis of the X_0-Y_0 frame [see Fig. 1(b)].

3.2. Generation of forward data

The thermo-optomechanical parameters like I_0, μ, β and C_P were taken as unity for each RBC [27]. The sound-speed was chosen as $v_s = v_f$ = 1500 m/s; the density was fixed to $\rho_s = \rho_f$ = 1000 kg/m^3. The contributions from a wide range of frequencies (1 to 1000 MHz with an increment of 1 MHz) were considered while evaluating Eq. (6) for a single cell. The PA signal was sampled at 2000 MHz. The sensors were placed at a distance r_d = 35 mm from the center of the imaging region [see Fig. 1(c)]. The position coordinates of cells relative to a detector could be determined by employing Eq. (16). After that, a long vector of length 100000 × 1 was initialized with zeros. The SIRF for each cell was computed sequentially at the same sampling frequency for that detector and added to this vector. The xdc_piston and calc_h functions of Field II were utilized for this purpose [33]. Subsequently, the PA signal for a single RBC was convolved with this long vector to generate the PA signal by the vasculature structure. This signal was filtered with a cosine Gabor filter mimicking the frequency response of a transducer with 2.25 MHz as the center frequency and 70% as the bandwidth. The next step was to downsample the PA signal 40 times [27]. This procedure was followed for 100 detector positions. The PA signals were simulated for two detectors with a diameter of 6 mm (computation time ≈ 2 hr 20 min) and 12 mm (execution time ≈ 13 h). The impact of the directivity of the sensor while collecting the tiny signals emitted by the individual cells was thus incorporated in this approach.

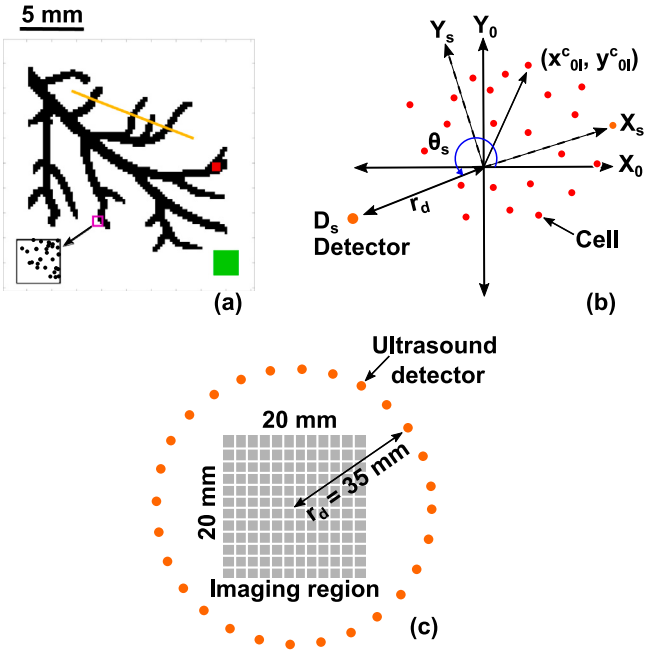

Fig. 1. (a) Vasculature phantom considered in this study. Inset displays the spatial organization of some cells/spheres belonging to the pink box. The pixels marked by red and green boxes represent the region of interest and background, respectively. Image profile has been generated along the golden line. (b) Cells are randomly distributed in space. X_0-Y_0 is the initial coordinate system and X_s-Y_s is the coordinate system for the detector D_s. (c) Schematic for PAT reconstruction. (For interpretation of the references to color in this figure legend, the reader is referred to the web version of this article.)

3.3. Image creation

The entire imaging region was divided into 101 × 101 grid points with $dx = dy = 200$ μm [see Fig. 1(c)]. Initially, the PA signal generated by a spherical source with 50 μm as the radius was calculated. The SIRF for a grid point and for a particular detector was also computed after the appropriate coordinate transformation. The convolution between this signal and SIRF was performed to obtain the PA signal generated by that grid point. Subsequently, this high-frequency signal was filtered and downsampled. The PA signals from all grid points for that detector were calculated and loaded into the M matrix. These steps were also followed for all detectors. In this manner, the M matrix was built for the FD WD method. The generation time for M matrix for 100 detectors was about 2 h 40 min for 6 mm and 3 h for 12 mm transducer. This protocol took care of the angular response of each sensor for each grid point while building the M matrix. The initial pressure rise was then estimated via Eq. (10). The cgsvd, l_curve, and tikhonov functions of the regularization toolbox were deployed for this purpose [29]. Image reconstructions were also performed for two other cases (PD and FD WOD) for comparison as stated earlier. For the PD scheme, the scaling and shifting properties of the PA signal (i.e., filtered and downsampled PA signal generated by the 50 μm sphere) were utilized for the formation of the M matrix (hence, the finite aperture size and directivity effect were not included in this approach). For the FD WOD case, we essentially followed the same procedure as that of the FD WD technique for the construction of the M matrix. However, only radial distances of the grid crossings from the centers of the sensors were considered while calculating the SIRFs. Therefore, the directivity factor was ignored in this case.

3.4. Quantitative comparison of reconstruction methods

Improving the quality of a digital image can be subjective. For example, claiming that one reconstruction method provides better images than the other can differ from one person to another. For this reason, image quality metrics have been developed to quantitatively assess the image enhancement algorithms [34]. Here, some commonly used image quality parameters were calculated to compare the performance of the reconstruction techniques [27]. For example, error norm (ERN), Pearson's correlation coefficient (PCC), and signal-to-noise ratio (SNR) were determined.

3.4.1. Error norm (ERN)

The ERN can be computed using the following relation,

$$\mathrm{ERN} = \|\mathscr{U} - \mathscr{U}_{sol}\|_2, \tag{17}$$

where $\mathscr{U}$ and $\mathscr{U}_{sol}$ are the nominal and reconstructed values, respectively. When $\mathscr{U}$ and $\mathscr{U}_{sol}$ are identical, the ERN becomes zero.

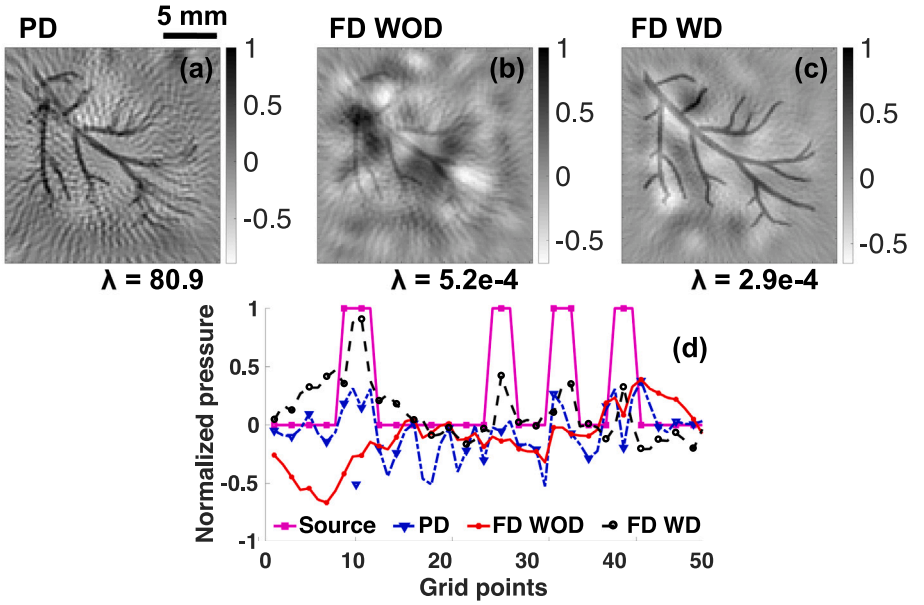

Fig. 2. Normalized (by the maximum pressure value) reconstructed images for the 6 mm transducer with scanning radius, $r_d = 35$ mm — (a) for point detector (PD), (b) for finite detector without considering directivity (FD WOD) and (c) for finite detector with directivity factor (FD WD). The numerical value of λ is given at the bottom of each figure. (d) The line plots along the golden line [see Fig. 1(a)] for the source and reconstructed images. (For interpretation of the references to color in this figure legend, the reader is referred to the web version of this article.)

3.4.2. Pearson's correlation coefficient (PCC)

The PCC is a measure of similarity between the ground truth and the reconstructed image. It can be calculated as,

$$\text{PCC} = \frac{\text{COV}(\mathscr{U}, \mathscr{U}_{sol})}{\sigma_{\mathscr{U}}\, \sigma_{\mathscr{U}_{sol}}}, \tag{18}$$

where COV, $\sigma_{\mathscr{U}}$, and $\sigma_{\mathscr{U}_{sol}}$ are the covariance between $\mathscr{U}$ and $\mathscr{U}_{sol}$ image matrices, standard deviation of $\mathscr{U}$ and standard deviation of $\mathscr{U}_{sol}$, respectively. The PCC value ranges from -1 to 1. Better reconstructions have PCC values closer to 1.

3.4.3. Signal to noise ratio (SNR)

The SNR is defined as,

$$\text{SNR} = 20 \log_{10} \left(\frac{A}{\sigma_{back}}\right), \tag{19}$$

where A is the peak pressure value in 'roi' and σ_{back} represents the standard deviation of 'back'. The 'roi' and 'back' [red and green regions as shown in Fig. 1(a)]. These areas spanned over 16 and 121 pixels, respectively.

4. Simulation results

Reconstructed images provided by the three methods (PD, FD WOD, and FD WD) are displayed in Fig. 2(a)–(c), respectively for the 6 mm sensor. Each figure is normalized by its maximum pressure value. The numerical value of the regularization parameter λ is given at the bottom of each figure. The respective line plots along the golden line [as given in Fig. 1(a)] are shown in Fig. 2(d). The same plot for the ground truth is also included in this figure for comparison. It is visually clear from Fig. 2 that image reconstructed using the FD WD method is of much better quality compared to those of PD and FD WOD protocols. Significant blurring occurs in the case of PD. Though the FD WOD scheme works well in the central region but fails to reproduce the vascular structure in the peripheral region. The background noise is significantly less in Fig. 2(c) than those in Fig. 2(a) and (b). In Fig. 2(d), good agreement in terms of peak matching between the FD WD and source lines (black and magenta lines, respectively) can be observed. Nevertheless, the lines for the PD (blue line) and FD WOD (red line) techniques do not exhibit a good match with the source line. The PA signal appears to have spread in the case of PD and FD WOD indicating the presence of blurring in the images. This blur was not present in the FD WD case. Similarly, the reconstructed images and line plots for the 12 mm transducer are included in Fig. 3. Here also, the FD WD provides faithful reconstruction. The bar charts in Fig. 4(a)–(c) show quantitative comparisons of the reconstruction methods. It can be seen that ERN is comparable for these methods [Fig. 4(a)]. However, PCC and SNR are remarkably higher for the FD WD with respect to the other methods (particularly, FD WOD) [see Fig. 4(b) and (c)]. This is true for both the transducers.

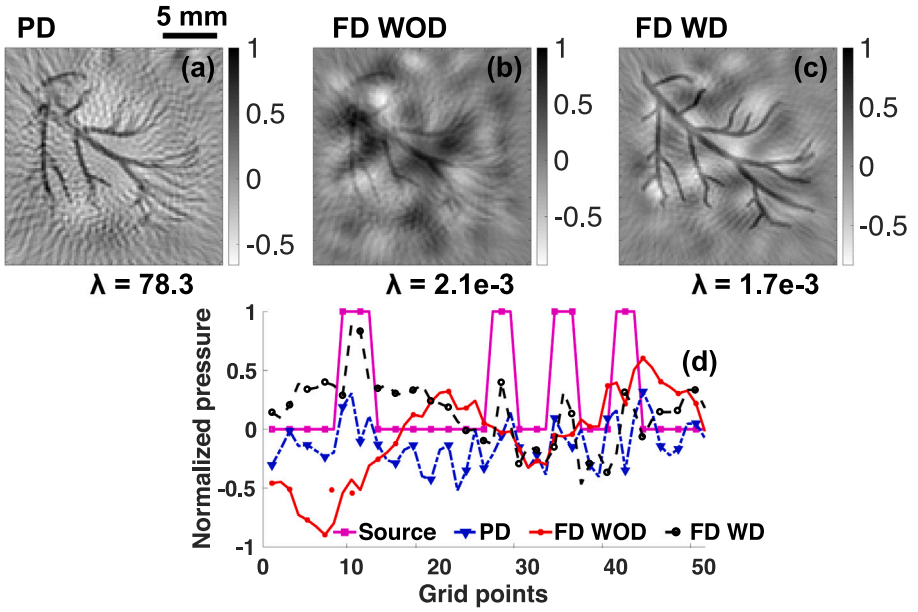

Fig. 3. Demonstration of the reconstructed images (normalized) for the 12 mm transducer (scanning radius, r_d = 35 mm) — (a) for point detector (PD), (b) for finite detector without taking into account directivity (FD WOD) and (c) for finite detector with directivity factor (FD WD). The numerical value of optimum λ is included at the bottom of each figure. (d) Comparison of image profiles drawn along the golden line [see Fig. 1(a)] for the original and reconstructed images. (For interpretation of the references to color in this figure legend, the reader is referred to the web version of this article.)

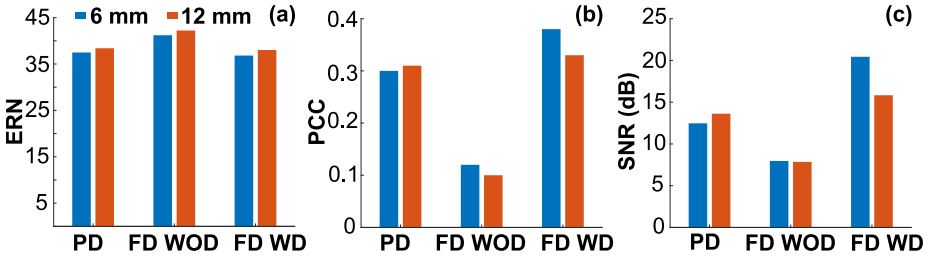

Fig. 4. Comparison of the error norm in (a), Pearson's correlation coefficient in (b), and the signal to noise ratio in (c) for different reconstruction schemes (PD, FD WOD, and FD WD) for both the transducers.

The reconstructed images have also been generated by varying the scanning radius of the sensors. The images (a)–(i) in Fig. 5 are the normalized images reconstructed using the PD, FD WOD, and FD WD methods, respectively (arranged in columns 1–3) for the 6 mm transducer. These images are placed from rows 1–3 for scanning radii- r_d = 25, 45 and 55 mm, respectively. The corresponding line plots are presented in Fig. 5(j)–(l) [drawn along the golden line in Fig. 1(a)]. It is visually evident from the images (column 1) that the directivity effect is dominant for smaller scanning radius i.e. r_d = 25 mm as compared to that of 45 and 55 mm radii. The branches of the vasculature phantom in the peripheral regions are better reconstructed for a larger scanning radius [see Fig. 5(g) and (h)]. The line plots [Fig. 5(j), (k), and (h)] also verify the same. The images in Fig. 6 are the same as those of Fig. 5 but reconstructed for the 12 mm transducer. The same trends can be observed. Nevertheless, the effect of directivity for the 12 mm detector is higher compared to that of the 6 mm transducer. The numerical study using the same image quality metrics ERN, PCC, and SNR have also been analyzed (data not shown). The numerical values are consistent with our findings.

5. Discussion and conclusions

A vasculature phantom was made using a Monte Carlo algorithm for sphere packing. For a sparse medium (i.e., in the physiological hematocrit level), it is a very fast method for blood tissue simulation. However, the RSA method may become slow for a dense system (e.g., when hematocrit is ≥ 0.5). The structural details of the tissue at the cellular level are retained in this approach. It also provides position coordinates of individual cells and thus exact calculation of SIRF corresponding to each cell is possible. Moreover, thermo-optomechanical properties, size, and shape parameters of individual sources can be incorporated during signal simulation. The convolution sum realistically models signal recording by a transducer with finite aperture. Therefore, it is a robust

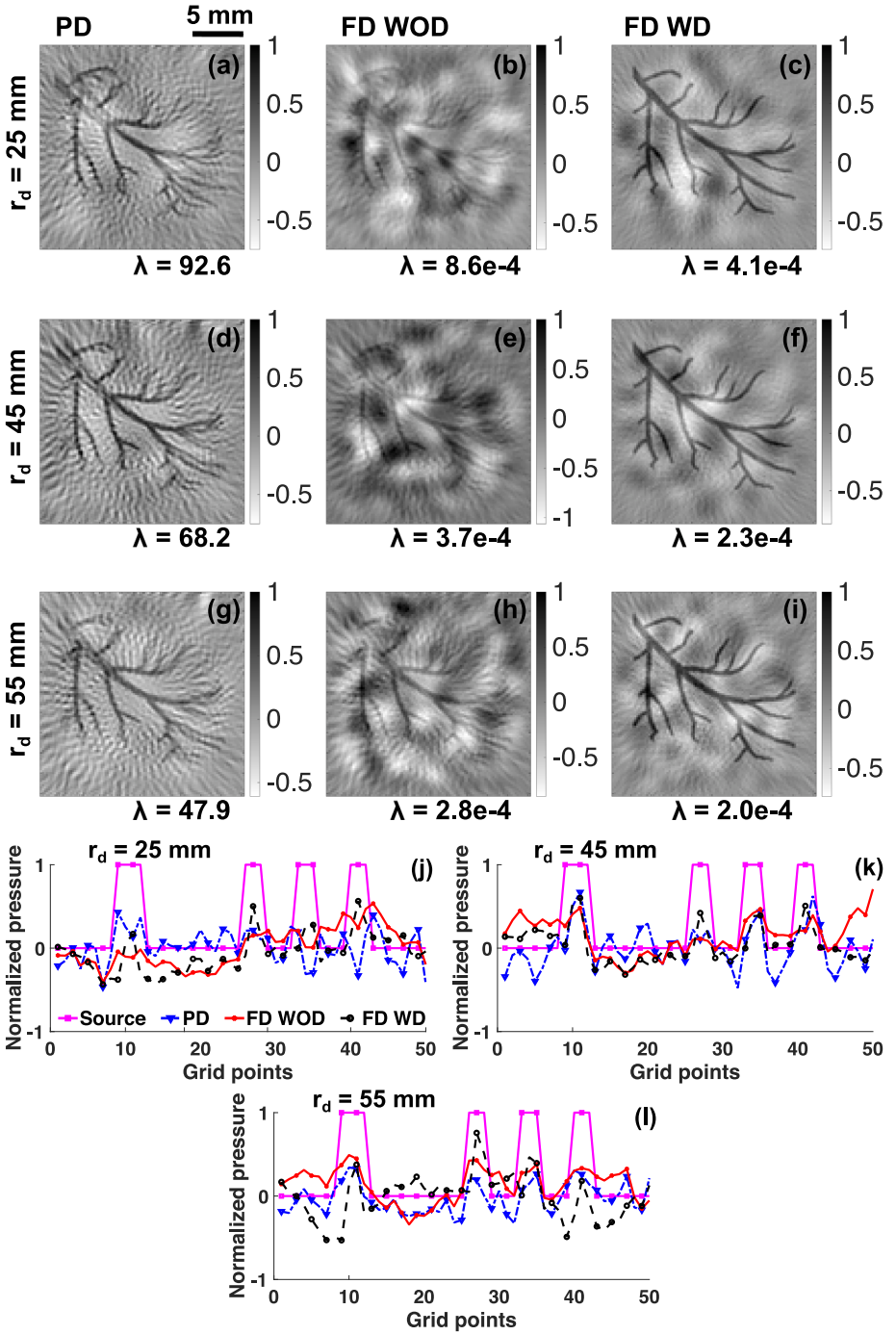

Fig. 5. (a)–(i) Normalized reconstructed images (columns 1–3 for PD, FD WOD, and FD WD methods, respectively) arranged in rows 1–3 for scanning radii r_d = 25, 45 and 55 mm, respectively. The corresponding line plots for these radii are given in (j)–(l) (drawn along the golden line in Fig. 1(a)) for the 6 mm transducer. (For interpretation of the references to color in this figure legend, the reader is referred to the web version of this article.)

framework for the forward signal simulation. Similarly, the PA response of each grid point for such a transducer can be faithfully (by including directivity factor) estimated and that can be loaded into the system matrix. It is intuitively expected that the effect of sensor directivity would be canceled out during matrix inversion procedure and hence PAT image reconstruction free from the negative effect of sensor directivity may be possible.

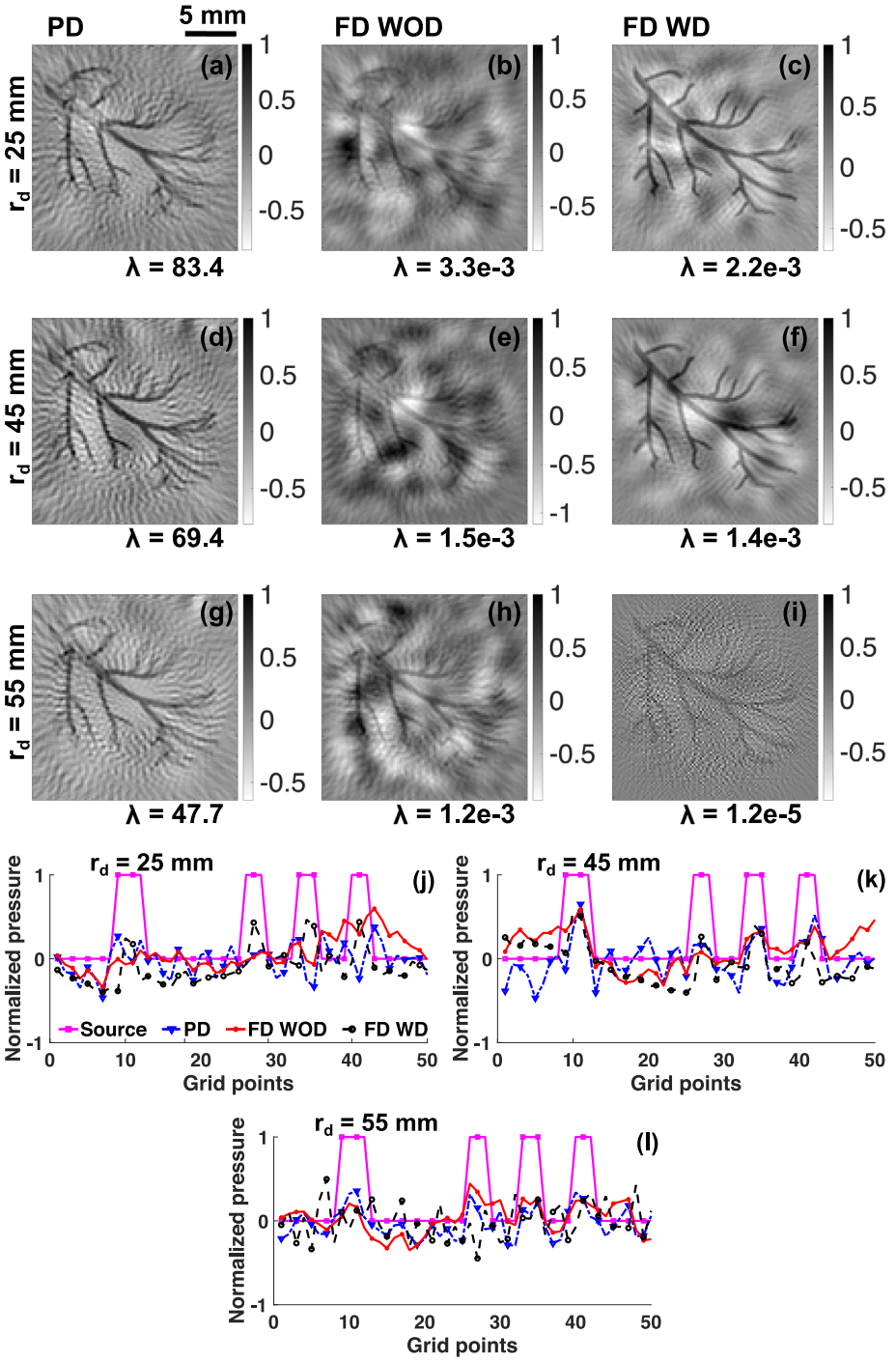

Fig. 6. Same as Fig. 5 but for the 12 mm transducer.

It is well known that significant blurring in the reconstructed images occurs for sensors with finite aperture size. However, it can be reduced significantly by increasing the scanning radius [see images (a), (d) and (g) of Figs. 5 and 6]. The simulation results presented herein are in accordance with this observation. Moreover, image blurring is less [see images (b), (e) and (h) of Figs. 5 and 6] for the FD WOD method compared to that of the PD scheme. In addition to that, image formation improves gradually as the scanning radius increases for the same method (i.e., peripheral regions of the vasculature structure are reproduced in a better

manner when the scanning radius is large). The negative effects of finite aperture size and directivity are both nullified in the case of FD WD protocol and it works well for all scanning radii [see images (c), (f) and (i) of Figs. 5 and 6].

As discussed earlier, a transducer with a finite aperture has two important properties — (i) the angular (the angle made by the position vector corresponding to a field point with respect to the axis of the transducer) response is not uniform and this is due to the diffraction phenomenon and (ii) it converts a narrow input pulse into a broad output pulse owing to the finite size of the aperture. Therefore, the impacts of these factors (depending upon the transducer used) are always embedded within a captured signal. The PD method assumed the detectors as point sensors with an omni-directional response to the incoming acoustic signals. Therefore, the PD method was unable to nullify the above mentioned effects during the image reconstruction and produced blurred images. The second factor was included while building the M matrix for the FD WOD method (but the first factor was not incorporated). That is why the FD WOD approach fairly recovered the vascular structure at the central region but failed for the peripheral regions (where the directivity effect is prominent). The FD WD method considered both the aspects while constructing the M matrix and that is why created significantly blur-free images. As implemented in this study, the M matrix for the FD WD scheme can be formed theoretically for the transducer in use (based on its specifications). The response of a transducer can be measured experimentally (e.g., utilizing a hydrophone) and accordingly, the M matrix can be built. Such a model matrix may facilitate system-independent image reconstruction.

In this work, the Tikhonov regularization method has been applied for image reconstruction. This approach has been extensively utilized by various groups [22,30]. Nevertheless, other algorithms such as l_1 regularization and total variation minimization techniques have also been employed for sparse data set and for improved image generation [30]. Most recently, it has been reported that fractional regularization can even provide better image reconstruction [30]. We plan to use these methods in the future and also attempts may be made to experimentally validate the findings of this study.

The proposed protocol emerges as a much superior method for PAT image reconstruction and outperforms other schemes. It can be confirmed through visual inspection of the reconstructed images (see Figs. 2 and 3) as well as from Fig. 4. For example, PCC and SNR values for FD WD are nearly 4 and 2 times higher than that of FD WOD, respectively. The simulation results suggest that the FD WD technique presented here can be utilized in practice for generating PAT images independent of transducer directivity.

Declaration of competing interest

The authors declare that they have no known competing financial interests or personal relationships that could have appeared to influence the work reported in this paper.

Acknowledgments

The computational results reported in this work were performed on the Central Computing Facility of IIIT Allahabad. This work was supported by an ICMR, India grant (# 56/2/2020-Hae/BMS).

References

[1] L.V. Wang, Photoacoustic Imaging and Spectroscopy, CRC Press, 2017.
[2] P.J. La Rivière, J. Zhang, M.A. Anastasio, Image reconstruction in optoacoustic tomography for dispersive acoustic media, Opt. Lett. 31 (6) (2006) 781–783.
[3] S. Liu, H. Wang, C. Zhang, J. Dong, S. Liu, R. Xu, C. Tian, In vivo photoacoustic sentinel lymph node imaging using clinically-approved carbon nanoparticles, IEEE Trans. Biomed. Eng. 67 (7) (2019) 2033–2042.
[4] H. Kim, J.H. Chang, Multimodal photoacoustic imaging as a tool for sentinel lymph node identification and biopsy guidance, Biomed. Eng. Lett. 8 (2) (2018) 183–191.
[5] P.K. Upputuri, M. Pramanik, Dynamic in vivo imaging of small animal brain using pulsed laser diode-based photoacoustic tomography system, J. Biomed. Opt. 22 (9) (2017) 090501.
[6] P. Rajendran, S. Sahu, R.A. Dienzo, M. Pramanik, In vivo detection of venous sinus distension due to intracranial hypotension in small animal using pulsed-laser-diode photoacoustic tomography, J. Biophotonics 13 (6) (2020) e201960162.
[7] L. Li, L.V. Wang, Recent advances in photoacoustic tomography, BME Front. 2021 (2021).
[8] J. Yao, L.V. Wang, Recent progress in photoacoustic molecular imaging, Curr. Opin. Chem. Biol. 45 (2018) 104–112.
[9] S. Guan, P.V. Chitnis, 3-D photoacoustic tomography reconstruction with deep learning for vasculature imaging, J. Acoust. Soc. Am. 148 (4) (2020) 2448.
[10] P.K. Upputuri, M. Pramanik, Recent advances toward preclinical and clinical translation of photoacoustic tomography: a review, J. Biomed. Opt. 22 (4) (2016) 041006.
[11] S. Manohar, M. Dantuma, Current and future trends in photoacoustic breast imaging, Photoacoustics 16 (2019) 100134.
[12] N. Nyayapathi, R. Lim, H. Zhang, W. Zheng, Y. Wang, M. Tiao, K.W. Oh, X.C. Fan, E. Bonaccio, K. Takabe, et al., Dual scan mammoscope (DSM)—a new portable photoacoustic breast imaging system with scanning in craniocaudal plane, IEEE Trans. Biomed. Eng. 67 (5) (2019) 1321–1327.
[13] S.E. Bohndiek, L.S. Sasportas, S. Machtaler, J.V. Jokerst, S. Hori, S.S. Gambhir, Photoacoustic tomography detects early vessel regression and normalization during ovarian tumor response to the antiangiogenic therapy trebananib, J. Nucl. Med. 56 (12) (2015) 1942–1947.
[14] S. Nandy, A. Mostafa, I.S. Hagemann, M.A. Powell, E. Amidi, K. Robinson, D.G. Mutch, C. Siegel, Q. Zhu, Evaluation of ovarian cancer: initial application of coregistered photoacoustic tomography and US, Radiology 289 (3) (2018) 740–747.
[15] M. Xu, L.V. Wang, Universal back-projection algorithm for photoacoustic computed tomography, Phys. Rev. E 71 (1) (2005) 016706.
[16] P. Warbal, M. Pramanik, R.K. Saha, Impact of sensor apodization on the tangential resolution in photoacoustic tomography, J. Opt. Soc. Amer. A 36 (2) (2019) 245–252.
[17] A.P. Rao, S. Sinha, Performance comparison of acoustic lens based photoacoustic image reconstruction with algorithm based reconstruction techniques, Optik (2021) 167512.
[18] B.E. Treeby, B.T. Cox, k-Wave: MATLAB toolbox for the simulation and reconstruction of photoacoustic wave fields, J. Biomed. Opt. 15 (2) (2010) 021314.
[19] G. Paltauf, J. Viator, S. Prahl, S. Jacques, Iterative reconstruction algorithm for optoacoustic imaging, J. Acoust. Soc. Am. 112 (4) (2002) 1536–1544.
[20] P. Warbal, R.K. Saha, Robust deblurring method in photoacoustic tomography involving system matrix, J. Modern Opt. (2021) Revision to be submitted.

[21] J. Prakash, A.S. Raju, C.B. Shaw, M. Pramanik, P.K. Yalavarthy, Basis pursuit deconvolution for improving model-based reconstructed images in photoacoustic tomography, Biomed. Opt. Express 5 (5) (2014) 1363–1377.
[22] A. Rosenthal, D. Razansky, V. Ntziachristos, Fast semi-analytical model-based acoustic inversion for quantitative optoacoustic tomography, IEEE Trans. Med. Imaging 29 (6) (2010) 1275–1285.
[23] Q. Kong, Q. Song, Y. Hai, R. Gong, J. Liu, X. Shao, Denoising signals for photoacoustic imaging in frequency domain based on empirical mode decomposition, Optik 160 (2018) 402–414.
[24] T.L. Szabo, Diagnostic Ultrasound Imaging: Inside Out, Academic Press, 2004, pp. 171–212.
[25] B. Cox, B. Treeby, Effect of sensor directionality on photoacoustic imaging: a study using the k-wave toolbox, in: Photons Plus Ultrasound: Imaging and Sensing, Vol. 7564, International Society for Optics and Photonics, 2010, p. 75640I.
[26] J. Huang, J.K. Triedman, N.V. Vasilyev, Y. Suematsu, R.O. Cleveland, P.E. Dupont, Imaging artifacts of medical instruments in ultrasound-guided interventions, J. Ultrasound Med. 26 (10) (2007) 1303–1322.
[27] R. Prakash, D. Badal, A. Paul, D. Sonker, R.K. Saha, Photoacoustic signal simulation using discrete particle approach and its application in tomography, IEEE Trans. Ultrason. Ferroelectr. Freq. Control 68 (3) (2021) 707–717.
[28] S. Karmakar, E. Hysi, M.C. Kolios, R.K. Saha, Realistic photoacoustic image simulations of collections of solid spheres using linear array transducer, in: Photons Plus Ultrasound: Imaging and Sensing 2015, Vol. 9323, International Society for Optics and Photonics, 2015, 932339.
[29] P.C. Hansen, Regularization tools version 4.0 for Matlab 7.3, Numer. Algorithms 46 (2) (2007) 189–194.
[30] J. Prakash, D. Sanny, S.K. Kalva, M. Pramanik, P.K. Yalavarthy, Fractional regularization to improve photoacoustic tomographic image reconstruction, IEEE Trans. Med. Imaging 38 (8) (2018) 1935–1947.
[31] R.K. Saha, Solving time-independent inhomogeneous optoacoustic wave equation numerically with a modified green's function approach, J. Acoust. Soc. Am. 149 (6) (2021) 4039–4048.
[32] J.G. Berryman, Random close packing of hard spheres and disks, Phys. Rev. A 27 (2) (1983) 1053–1061.
[33] J.A. Jensen, N.B. Svendsen, Calculation of pressure fields from arbitrarily shaped, apodized, and excited ultrasound transducers, IEEE Trans. Ultrason. Ferroelectr. Freq. Control 39 (2) (1992) 262–267.
[34] K.-H. Thung, P. Raveendran, A survey of image quality measures, in: 2009 International Conference for Technical Postgraduates, TECHPOS, IEEE, 2009, pp. 1–4.